ACS Energy LETTERS

http://pubs.acs.org/journal/aelccp

Efficient Scalable Hydrothermal Synthesis of MnO_2 with Controlled Polymorphs and Morphologies for Enhanced Battery Cathodes

Shifeng Hong,[†] Shuo Jin,[†] Yue Deng, Regina Garcia-Mendez, Keun-il Kim, Nyalaliska Utomo, and Lynden A. Archer*

Cite This: *ACS Energy Lett.* 2023, 8, 1744−1751

Read Online

ACCESS | Metrics & More | Article Recommendations | Supporting Information

ABSTRACT: **MnO_2 is a versatile, cost-effective transition metal oxide that has attracted interest in multiple domains, including as an active cathode material or catalyst for electrochemical energy storage in batteries. Hydrothermal methods are among the most efficient approaches for MnO_2 synthesis. These approaches enable facile, versatile production of MnO_2 in any of its crystalline phases (α, β, δ, etc.), with the dominant product being determined by reaction conditions such as precursor concentration and temperature. These benefits unfortunately come with impractically low product yields (~9%) and long reaction times. Here, we report that low-molecular weight, water-soluble polymers function as effective nucleating agents for the hydrothermal synthesis of MnO_2. For fundamental reasons, these polymers are also reported to promote large (10- to 40-fold) increases in reaction rate and yield. We evaluate the physical and crystallographic features of the synthesized MnO_2 and find that depending upon the reaction conditions, the polymer-assisted synthesis yields dominantly δ-MnO_2 or β-MnO_2. The as-prepared δ-MnO_2 materials with extra interlayer water are studied as electrodes for aqueous Zn-ion battery applications and are shown to support long-duration storage at both moderate and high rates.**

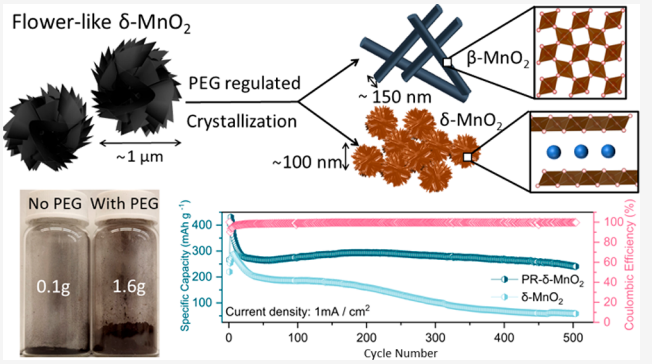

Manganese oxide (MnO_2) is a transition metal oxide material, which by virtue of its low cost, high earth abundance (Mn is the fifth most abundant metal in the earth's crust), and chemical versatility has attracted interest in an increasingly wider range of technologies.[1−5] MnO_2 has for example been demonstrated as an electrode material for energy storage in batteries and pseudocapacitors,[6−13] as an adsorbent/ion-exchange medium in air and water treatment,[2,14,15] and as a catalyst for organic synthesis.[2]

MnO_2 has likewise enjoyed a long history as an essential and versatile electrode component in dry cell batteries.[8] Notably, different polymorphs of MnO_2 show potential as electrode materials in batteries with working ions in a range of sizes and chemistries (e.g., Zn, Li, Na, K, Al, etc.). A large body of research over the last four decades has shown that MnO_2's promise as an electrode material is in fact limited neither to dry cell nor to primary batteries.[16−21] Two recent examples—the industrial-scale utilization of MnO_2, either alone or as a component, in the cathode for rechargeable lithium-ion batteries (LIBs) that offer higher average discharge voltage and improved specific capacity; and the growing use of layered δ-MnO_2 in aqueous Zn-ion batteries (ZIB) where it has been reported to facilitate a rapid ion diffusion kinetics for Zn in ZIBs [18,22−24]—illustrate the broad promise of the material.

Multiple chemical and electrochemical pathways, including electrodeposition,[5] sol−gel methods,[25] and microwave-assisted synthesis,[26] have been developed to synthesize MnO_2 in the specific crystal phases required for each of the various applications. Hydrothermal synthesis nonetheless stands out as being one of the most versatile and used synthesis methods for large-scale synthesis of MnO_2 structures in a variety of form factors and mass distributions (e.g., hollow, core−shell, rattles, etc.).[2,27−29] Advantages of the hydrothermal method are manifold and important: (i) Synthesis and crystallization can

Received: January 3, 2023
Accepted: March 9, 2023

https://doi.org/10.1021/acsenergylett.3c00018
ACS Energy Lett. 2023, 8, 1744−1751

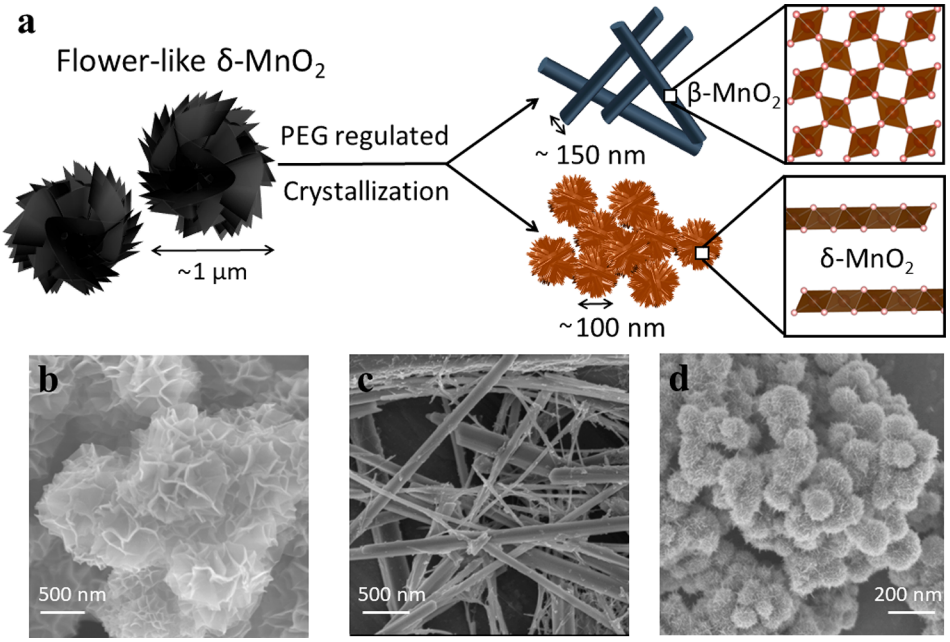

Figure 1. Morphology changes of MnO_2 synthesized with PEG additive. (a) Schematic illustration of PEG-regulated synthesis of PR-δ-MnO_2 and PR-β-MnO_2. Scanning electron microscopy (SEM) images of (b) pristine δ-MnO_2, (c) PR-β-MnO_2, and (d) PR-δ-MnO_2.

occur in a single step: compared with other synthesis pathways that require several separated steps, the hydrothermal method offers a simple one-pot synthesis. (ii) The dominant polymorphs produced can be controlled by straightforward changes in the synthesis conditions: different phases of MnO_2 (e.g., α, β, δ, etc.) can be acquired by adjusting temperature and precursor concentrations used in the synthesis.[30] (iii) Although some solid-phase methods have been reported to offer a high product yield, the synthesized product often contains non-negligible quantities of impurities, and the particle size is uncontrolled: hydrothermal synthesis, in contrast, has been reported to provide stable crystal structures with high crystallinity and narrow particle size distributions.[2,31] Notwithstanding these advantages, the low MnO_2 yield and long reaction times associated with hydrothermal synthesis methods are significant drawbacks. Several strategies have been reported to overcome these shortcomings of the hydrothermal synthesis, including the work by Whittingham et al.,[7] which showed that addition of 4 M HNO_3 to neutralize the produced KOH increases yield of δ-MnO_2 to over 90%. However, the reaction kinetics remain sluggish, and the high yields are achieved for long reaction times, e.g., 4 days.

A significant body of work has shown that regulation of the size of the MnO_2 particles is important for achieving stable, long-duration charge−discharge cycling in rechargeable batteries.[5,32−35] Meng et al.,[36] for example, reported that decreasing the average particle size of MnO_2 to nanoscale dimensions improves electrochemical performance. This finding apparently comes from two interrelated phenomena: (i) the increased specific surface area achieved at smaller particle sizes improves interfacial contact between electrolyte and electrode particles; and (ii) the smaller particle sizes result in shorter ion diffusion path lengths, which alleviate the problem of the relatively low ionic conductivity of MnO_2.[23]

Water-soluble polymers like poly(ethylene oxide) are known to physisorb strongly on specific crystallographic facets exposed on the surface of metal oxide nanoparticles.[37−40] At high molecular weights and particle concentrations, the polymers are also known to cause particle−particle aggregation and flocculation through a bridging effect.[41−43] An open question is whether low-molecular weight versions of these polymers might be able to form dynamic coordination with a growing metal oxide nanostructure to favor nucleation and catalyze growth of during hydrothermal synthesis. Herein, we evaluate this question using water-soluble PEG additives in the hydrothermal synthesis of MnO_2. We find that at concentrations as low as 0.05 wt %, PEG with $M_w \approx 3$ kDa increases both the yield (from approximately 9% to 97%) and reaction rate (from 4 days to 4 h reaction time) for hydrothermal synthesis of δ-MnO_2. Under some conditions the resultant material (denoted as PR-δ-MnO_2) exhibits smaller particle size, and under other reaction conditions PEG-regulated β-MnO_2 nanorods (denoted as PR-β -MnO_2) were obtained. Evaluation of the synthesized PR-δ-MnO_2 as the active material in the positive electrode of aqueous zinc-ion batteries revealed large improvements in long-term cycling stability and storage capacity due to significantly increased interlayer water brought by PEG. Additionally, based on literature reports,[44−46] we also analyzed the potential of the synthesized PR-β-MnO_2 as a cathode material in sodium metal batteries. For brevity, we focus mainly on the synthesis, analysis, and application of the PR-δ-MnO_2 material.

Figure 1a reports our findings for hydrothermal synthesis runs without and with PEG (M_w = 3 kDa, PEG 3000) at different concentrations. A key finding is that the characteristic flower-like δ-MnO_2 particles are formed in the absence of PEG, PR-β-MnO_2 nanorods are formed at relatively high concentration of PEG 3000, and urchin-shaped PR-δ-MnO_2 with smaller particle size are obtained at lower concentration of PEG 3000. As shown in Figure S1, the PR-δ-MnO_2 powder shows a brownish color while the δ-MnO_2 powder is black. Scanning electron microscopy (SEM) images (Figure 1b) show that conventional δ-MnO_2 formed in the absence of PEG exhibits an approximate spherical structure surrounded by

https://doi.org/10.1021/acsenergylett.3c00018
ACS Energy Lett. 2023, 8, 1744−1751

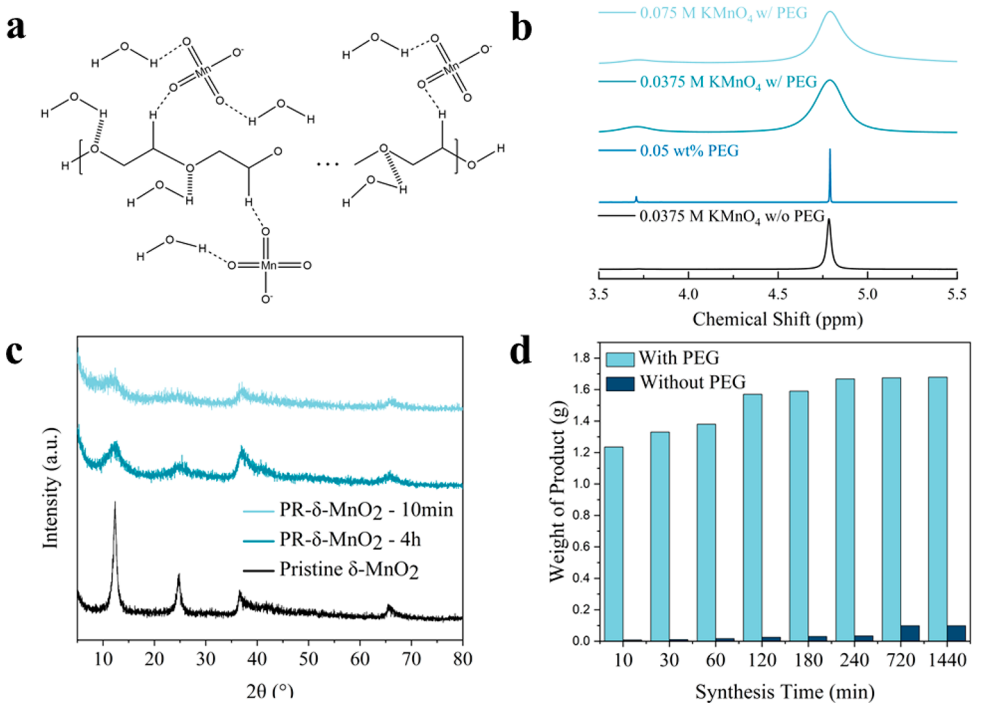

Figure 2. Design principle and proposed reaction mechanism. (a) PEG 3000 coordinates with water molecule and permanganate ions in the precursor solution for synthesizing PR-δ-MnO_2. (b) Nuclear magnetic resonance (NMR) spectrum of 0.0375 M $KMnO_4$, 0.05 wt % PEG 3000 solution, and 0.05 wt % PEG 3000 solution with different concentrations of $KMnO_4$. (c) X-ray diffraction (XRD) analysis of pristine δ-MnO_2 and PR-δ-MnO_2 with different synthesis time (10 min and 4 h). (d) Yield of δ-MnO_2 with and without PEG 3000 additive collected at different synthesis time.

petal-like flakes with average particle size in the range of 1.5−2 μm. However, with the additional PEG 3000 in precursor solution and other synthesis conditions maintained the same, the polymorph of MnO_2 can be changed and the morphology altered dramatically as well. Additional 0.05 wt % of PEG3000 in precursor solution produces urchin-shaped PR-δ-MnO_2 with average particle size of around 100 nm. Higher concentrations of PEG 3000 (0.1 wt % and higher) provide PR-β-MnO_2 nanorods whose diameter varies from 150 to 200 nm. It is speculated that the decreased particle size and urchin-shaped structure will contribute to boosting the material's specific surface area, which benefits its electrochemical performance. Brunauer−Emmett−Teller (BET) analysis was conducted to quantify the specific surface area increment; as shown in Figure S2, the pristine δ-MnO_2 shows a specific surface area of 9.90 m^2/g, while PR-δ-MnO_2 has an obvious, higher value of approximately 45.68 m^2/g.

As a first step toward understanding the large effect of PEG 3000 on the crystallographic and morphological features of MnO_2, we conjectured that the polymer in solution may serve as both a dispersant and linker for particle nuclei. Specifically, as a hydrophilic molecule, the oxygen in the PEG repeating units is thought to offer multiple, concatenated sites for hydrogen bonding. The relatively hydrophobic hydrogen in the PEG repeating units may conversely associate strongly with the oxygen in the permanganate anion. As shown in Figure 2a, PEG functions somewhat like a linker, such that permanganate anions and water molecules coordinate alternatively with the PEG3000 chain. We speculate that this prelinked structure helps reduce the migration energy barrier of permanganate ions during the nucleation process and may also hinder MnO_2 particle growth, causing the decreased particle size of PR-δ-MnO_2.

To evaluate the accuracy of the hypothesized prelinked structure, nuclear magnetic resonance (NMR) analysis were conducted. As shown in Figure 2b, the lower peak and the higher peak in the top three lines represent hydrogen in PEG repeating unit and hydrogen in water, respectively. It is speculated that the low intensity of the PEG peak is due to the small additive amount (0.05 wt %). After adding the same concentration of $KMnO_4$ as we used for δ-MnO_2 synthesis, both peaks become significantly broader, indicating a more sluggish proton motion.[47−49] By forming bonds with MnO_4^-, the hydrogens in water and PEG are less sensitive to the magnetic filed. Additionally, after calibration, there is a slight upfield shift of the PEG hydrogen peak with increasing MnO_4^- concentrations (Figure S3), which is also consistent with our hypothesis. Coordinating to MnO_4^-, the hydrogens in PEG repeating units were deshielded because the electronegatively of oxygen is higher than that of hydrogen. The NMR data therefore implies that the large effect of PEG 3000 on MnO_2 morphology likely arises from its ability to regulate the molecular arrangement in the precursor solution. Furthermore, according to the Raman spectroscopy analysis shown in Figure S4, the water environment is different among 0.05 wt % PEG solution, 0.0375 M $KMnO_4$, and 0.0375 M $KMnO_4$ in 0.05 wt % PEG solution.

Instead of random nucleation, the crystallization achieved in the presence of PEG results in a noticeably higher reaction rate and improved yield. Results from X-ray powder diffraction analysis reported in Figure 2c reveal that the material synthesized with low-concentration PEG 3000 has the same crystal framework as δ-MnO_2; PR-δ-MnO_2 produced after 10 min and 4 h of synthesis exhibits peaks that have identical 2θ locations with the pristine δ-MnO_2. Nevertheless, PR-δ-MnO_2 shows broader (001) and (002) peaks, which could be

https://doi.org/10.1021/acsenergylett.3c00018
ACS Energy Lett. 2023, 8, 1744−1751

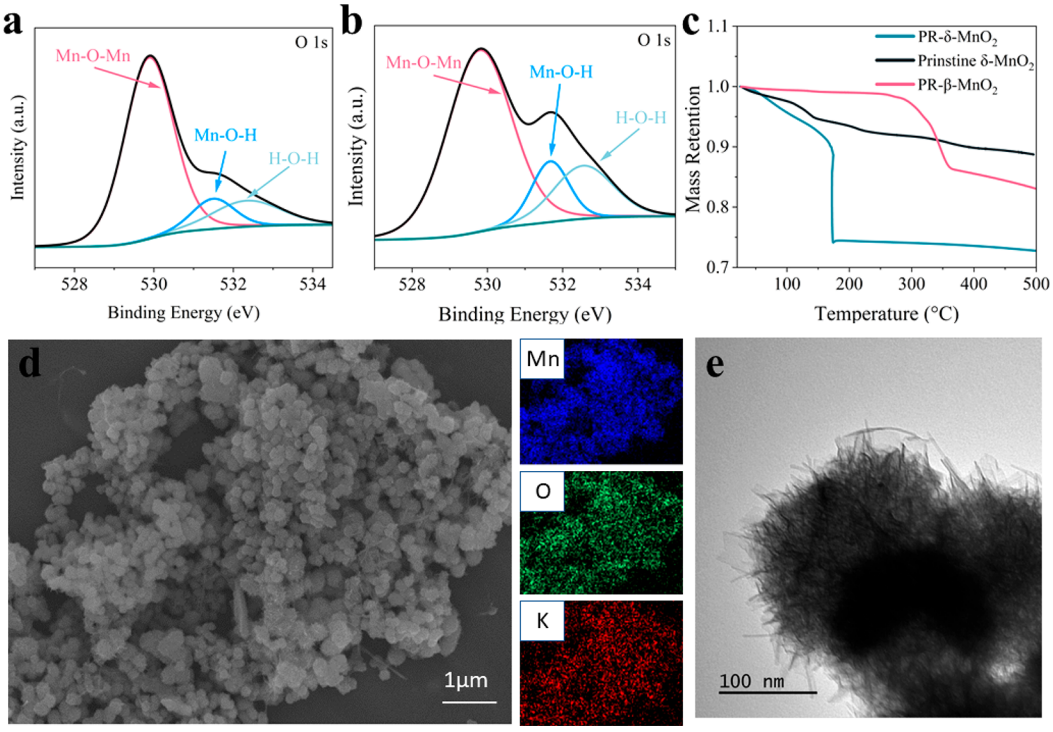

Figure 3. Material characterization and analysis. X-ray photoelectron spectra of (a) δ-MnO_2 and (b) PR-δ-MnO_2. (c) Thermogravimetric analysis of pristine δ-MnO_2, PR-δ-MnO_2, and PR-β-MnO_2. (d) Energy-dispersive X-ray spectroscopy mapping of PR-δ-MnO_2. (e) Transmission electron microscopy (TEM) image of PR-δ-MnO_2.

attributed to the formation of nanosized crystals.[5] According to the Scherrer equation, line broadness at half the maximum intensity is inversely proportional to the mean size of the crystalline domains.[50] Additionally, Figure S5 shows the synthesized PR-β-MnO_2 has the same structure as pristine β-MnO_2 with limited impurity peaks. A series of syntheses was conducted to probe the relation between reaction time and PR-δ-MnO_2 yield. All the reaction conditions, including reactor size, precursor mass, and synthesis temperature, are maintained identical; the only difference is with or without the PEG 3000 additive. As shown in Figure 2d, 0.05 wt % of PEG 3000 additive dramatically increases the yield as well as the reaction rate of hydrolysis reaction of producing δ-MnO_2. It is observed that the yield of PR-δ-MnO_2 saturated after 4 h of synthesis. Results reported in Figure S6 for higher PEG3000 concentrations show that the polymer has a similar effect on the β-phase MnO_2.

We investigated the effect of PEG molecular weight on the yield and reaction kinetics of the hydrothermal synthesis. In these experiments, the PEG concentration in the precursor solution was held fixed at 0.05 wt % and the molecular weight varied from 3000 to 20,000. The results reported in Figures S7−S9 indicate that there is not an obvious difference in the yield, structure, or particle morphology. On this basis, we selected PEG3000 as the additive material for the in-depth physical and electrochemical analysis of the hydrothermally synthesized MnO_2 materials.

X-ray photoelectron spectroscopy (XPS) was performed to investigate the bonding information on synthesized PR-δ-MnO_2. As shown in Figure 3a,b, the deconvoluted δ-MnO_2 O 1s spectra show three peaks at 529.8, 531.5, and 532.4 eV, which correspond to Mn−O−Mn, Mn−O−H, and H−O−H bonds.[51] A significant increased intensity and area of Mn−O−H and H−O−H bonds was found on the PR-δ-MnO_2 O 1s spectra, indicating more water molecules were bonded in the interlayer of PR-δ-MnO_2. Additionally, the thermogravimetric analysis (TGA) outcome is consistent with the XPS results. As shown Figure 3c, there is a ∼15% weight loss of PR-δ-MnO_2 at 170 °C, which was reported to be the evaporation of bonded crystal water,[7] while the pristine δ-MnO_2 yields a much lower weight loss at 170 °C as shown in Figure S10. To further prove that extra water content exists in the PR-δ-MnO_2 interlayers, XRD was conducted on PR-δ-MnO_2 which has been heated at 180 °C in a dry environment for 12 h to ensure the evaporation of structural water. As shown in Figure S11, the (001) and (002) peaks showed a slight right-shift which corresponds to a decreased interlayer spacing. Thus, the water molecules were believed to be located between the layers of PR-δ-MnO_2 according to the XPS, TGA, and XRD results.

Previous literature reported that PEG degrades between 300 and 400 °C in TGA;[52,53] our TGA results shown in Figure S12 is consistent with these reports. As shown in Figure 3c, PR-β-MnO_2 shows no significant weight loss at around 170 °C, while a ∼15% weight loss was observed between 300 and 400 °C, corresponding to the degradation of PEG. In contrast, no obvious weight loss between 300 and 400 °C was found for PR-δ-MnO_2 whose PEG additive amount is half of the amount for PR-β-MnO_2. Therefore, we believe that PEG does not exist in the synthesized PR-δ-MnO_2.

Energy-dispersive X-ray spectroscopy (EDS) mapping was conducted to probe the spatial distribution of manganese, oxygen, and intercalated potassium. According to Figure 3d, the synthesized particles have a uniform distribution of Mn, O, and K. To further determine the exact chemical formula of PR-δ-MnO_2, laser ablation inductively coupled plasma optical emission spectroscopy (LA-ICP-OES) analysis was performed. Combined with the TGA result, the determined formula for synthesized pristine δ-MnO_2 and PR-δ-MnO_2 is $K_{0.175}MnO_2$·

https://doi.org/10.1021/acsenergylett.3c00018
ACS Energy Lett. 2023, 8, 1744−1751

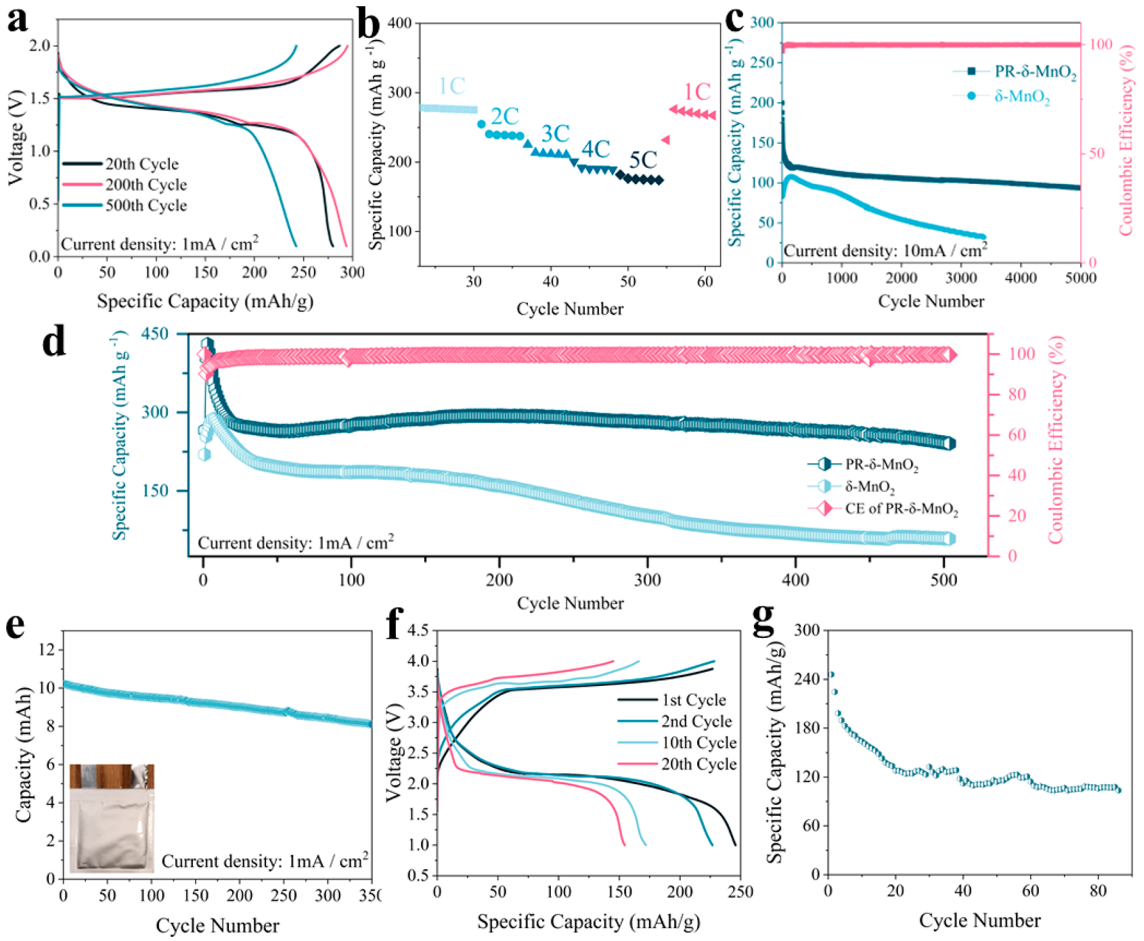

Figure 4. Electrochemical analysis of MnO_2. (a) Discharge profile of Zn | 2 M $ZnSO_4$ + 0.2 M $MnSO_4$ | PR-δ-MnO_2 coin cell at 1 mA/cm^2. (b) Rate stability analysis of PR-δ-MnO_2 coin cell. Cycling performance of Zn | 2 M $ZnSO_4$ + 0.2 M $MnSO_4$ | PR-δ-MnO_2 coin cell at different current density: (c) 10 mA/cm^2 and (d) 1 mA/cm^2. (e) Pouch cell cycling performance after activation cycles. (h) Discharge profile of Na | 1 M $NaClO_4$ in EC/PC (50:50 v: (v) | PR-β-MnO_2 coin cell (0.1C). (g) Cycling performance of Na | 1 M $NaClO_4$ in EC/PC (50:50 v:v) | PR-β-MnO_2 coin cell (0.2C).

$0.16H_2O$ and $K_{0.126}MnO_2{\cdot}1.11H_2O$. Additionally, the transmission electron microscopy (TEM) images in Figure 3e further prove the urchin-like morphology of PR-δ-MnO_2, which is consistent with specific surface area increment. The characterization results discussed above revealed that PR-δ-MnO_2 has smaller particle size, higher specific surface area, and significantly increased interlayer water. In the following, PR-δ-MnO_2 is shown to be a superior cathode material for a zinc-ion battery for hosting protons and zinc ions owing to its special features.

Here, we evaluated PR-δ-MnO_2 as the cathode material in Zn | 2 M $ZnSO_4$ + 0.2 M $MnSO_4$ | PR-δ-MnO_2 coin cells and pouch cells. Galvanostatic charge/discharge (GCD) profiles of Zn | 2 M $ZnSO_4$ + 0.2 M $MnSO_4$ | PR-δ-MnO_2 coin cells are presented in Figure 4a. It shows a typical Zn-MnO_2 discharge profile, which consists of one plateau at around 1.45 V corresponding to proton intercalation and another plateau at around 1.3 V corresponding to zinc-ion intercalation. According to the cyclic voltammetry results shown in Figure S13, there are two pairs of redox peaks for both PR-δ-MnO_2 and δ-MnO_2. The observed results are consistent with previously reported proton−zinc sequential intercalation theory.[5] Notably, PR-δ-MnO_2 provides a significantly increased capacity (295 mAh/g) which approaches the theoretical value of δ-MnO_2 (308 mAh/g). It is tentatively believed that the previously demonstrated decreased average particle size and higher specific surface area are responsible for the dramatic capacity change because both ensure a broader electrolyte/electrode interface that increases possible reaction sites. A rate stability test was conducted, and the results are shown in Figure 4b; stable capacity was maintained from 1C to 5C and back to 1C. Figure 4c compares the performance of aqueous Zn-MnO_2 coin cells based on δ-MnO_2 and PR-δ-MnO_2 as the active material in the cathode under a high current density of 10 mA/cm^2. After the first few activation cycles, the cell can offer a ∼120 mAh/g specific capacity and cycle 5000 times with 80% retention. Pristine δ-MnO_2 whose capacity fades rapidly shows a limited high-current capability. Previous reports indicate that additional water molecules in the interlayer help boost the proton intercalation according to the Grotthuss mechanism and the zinc-ion intercalation via electrostatic shielding, which could be a reason for the significantly improved rate capability.[54−57] Thus, the galvanostatic intermittent titration technique (GITT) was applied to quantify the proton and zinc cation diffusivity. The analysis results are plotted in Figure S14a, and the calculated diffusivity in Figure S14b versus the ion insertion state reveals that PR-δ-MnO_2 has a higher diffusion rate both for protons and for zinc ions in solution. It is already known that a fast ion diffusion rate allows the cathode to have high-current capability.

https://doi.org/10.1021/acsenergylett.3c00018
ACS Energy Lett. 2023, 8, 1744−1751

In Figure 4d, it is apparent that significant capacity fade both during and after the first hundred charge/discharge cycles is a characteristic of the δ-MnO_2 not shared with PR-δ-MnO_2. The latter instead manifests a stable plateau at around 290 mAh/g for 500 cycles (976 h). We note further that the end-of-life of these batteries is not limited by the MnO_2 cathode but rather arises from failure of the Zn anode due to short-circuit caused by dendritic growth of the zinc anode. A significant body of work has studied the effect of interlayer ions and molecules on stabilizing a layered material structure.[54−56] It was shown above that PR-δ-MnO_2 has a unique water-rich interlayer; the extra interlayer water is speculated to reduce electrostatic interactions between working ions and PR-δ-MnO_2 and also pillaring of the layered structure.[55] Thus, PR-δ-MnO_2 exhibits a more stable cycling performance under a low current density.

Furthermore, owing to the benefits of fast and efficient production of PR-δ-MnO_2, a Zn | 2 M $ZnSO_4$ + 0.2 M $MnSO_4$ | PR-δ-MnO_2 pouch cell was assembled. As shown in Figure 4e, after activation cycles, a 3 × 3 cm pouch cell can cycle over 350 times with 75% capacity retention. At last, sodium metal batteries paired with a PR-β-MnO_2 cathode were assembled and analyzed. As shown in Figures 4f and S15, a flat discharge plateau at around 2.3 V was observed in the discharge profile of the Na || PR-β-MnO_2 coin cell. Figure 4g shows that the Na || PR-β-MnO_2 coin cell can offer a stabilized discharge capacity at around 120 mAh/g and cycle more than 80 times at a slow charge/discharge rate (0.2C).

In summary, we report that introduction of even a small amount of the water-soluble polymer (PEG 3000) in a hydrothermal synthesis dramatically enhances the reaction rate and yield of δ-MnO_2 and β-MnO_2. The polymer is shown to act as a linker, which appears to regulate the arrangement of molecules in the precursor solution, which is believed to lower the energy barrier for nucleation and refinement of MnO_2 crystal growth. We analyzed the as-synthesized PR-δ-MnO_2 in detail and found that the polymer-assisted product also offers smaller average particle sizes, higher specific surface area, and a water-rich interlayer. All of these features enhance PR-δ-MnO_2's potential as a cathode material in aqueous zinc-ion batteries. We evaluate this potential in electrochemical cells in which Zn anodes are paired with a PR-δ-MnO_2 cathode (e.g., Zn | 2 M $ZnSO_4$ + 0.2 M $MnSO_4$ | PR-δ-MnO_2 cells). The cells are reported to manifest increased specific capacity, high current density capability, and good long-term stability in galvanostatic cycling at moderate rates. We also report that PR-β-MnO_2 has potential to serve as a cathode in sodium metal batteries. We conclude that the reported polymer-assisted hydrothermal approach paves a path toward a scalable strategy for synthesizing δ-MnO_2 and β-MnO_2 on a large scale for use in zinc-ion batteries and sodium-ion batteries.

■ ASSOCIATED CONTENT

Supporting Information

The Supporting Information is available free of charge at https://pubs.acs.org/doi/10.1021/acsenergylett.3c00018.

Materials, synthesis methods, physical and electrochemical analysis methods, picture of PR-δ-MnO_2 and δ-MnO_2, BET analysis results, NMR chemical shifts, Raman analysis, XRD of PR-β-MnO_2, analysis of PR-δ-MnO_2 synthesized with different molecular weight, XRD results of PR-δ-MnO_2 with and without structural water, TGA analysis of PEG 3000, CV and GITT analysis of Zn || PR-δ-MnO_2, discharge profile of Nal1 M $NaClO_4$ in EC/PC (50:50 v:v) | PR-β-MnO_2 (PDF)

■ AUTHOR INFORMATION

Corresponding Author

Lynden A. Archer − *Department of Materials Science and Engineering, Cornell University, Ithaca, New York 14853, United States; Robert Frederick Smith School of Chemical and Biomolecular Engineering, Cornell University, Ithaca, New York 14853, United States;* orcid.org/0000-0001-9032-2772; Email: laa25@cornell.edu

Authors

Shifeng Hong − *Department of Materials Science and Engineering, Cornell University, Ithaca, New York 14853, United States*

Shuo Jin − *Robert Frederick Smith School of Chemical and Biomolecular Engineering, Cornell University, Ithaca, New York 14853, United States;* orcid.org/0000-0003-0425-9143

Yue Deng − *Department of Materials Science and Engineering, Cornell University, Ithaca, New York 14853, United States*

Regina Garcia-Mendez − *Robert Frederick Smith School of Chemical and Biomolecular Engineering, Cornell University, Ithaca, New York 14853, United States;* orcid.org/0000-0002-0980-3673

Keun-il Kim − *Robert Frederick Smith School of Chemical and Biomolecular Engineering, Cornell University, Ithaca, New York 14853, United States*

Nyalaliska Utomo − *Robert Frederick Smith School of Chemical and Biomolecular Engineering, Cornell University, Ithaca, New York 14853, United States;* orcid.org/0000-0001-8855-6297

Complete contact information is available at: https://pubs.acs.org/10.1021/acsenergylett.3c00018

Author Contributions

†S.H. and S.J. contributed equally to this work.

Notes

The authors declare no competing financial interest.

■ ACKNOWLEDGMENTS

This work was supported as part of the Center for Mesoscale Transport Properties, an Energy Frontier Research Center supported by the U.S. Department of Energy, Office of Science, Basic Energy Sciences, under award #DE-SC0012673. We also acknowledge support from DOE BES under award #DE-SC0016082. This work made use of the Cornell Center for Materials Research Shared Facilities which are supported through the NSF MRSEC program (DMR-1719875). The authors express their gratitude to Pengyu Chen and Ziang Gao for valuable discussions.

■ REFERENCES

(1) Yang, G.; et al. Hollow MnO_2 as a tumor-microenvironment-responsive biodegradable nano-platform for combination therapy favoring antitumor immune responses. *Nat. Commun.* **2017**, *8* (1), 902.

(2) Baral, A.; et al. A review of recent progress on nano MnO2: synthesis, surface modification and applications. *Journal of Inorganic and Organometallic Polymers and Materials* **2021**, *31* (3), 899−922.

(3) Guo, S.; et al. A High-Capacity, Low-Cost Layered Sodium Manganese Oxide Material as Cathode for Sodium-Ion Batteries. *ChemSusChem* **2014**, *7* (8), 2115−2119.
(4) Kozawa, A.; Powers, R. Electrochemical reactions in batteries. Emphasizing the MnO2 cathode of dry cells. *J. Chem. Educ.* **1972**, *49* (9), 587.
(5) Sun, W.; et al. Zn/MnO2 battery chemistry with H+ and Zn2+ coinsertion. *J. Am. Chem. Soc.* **2017**, *139* (29), 9775−9778.
(6) Jin, S.; et al. Production of fast-charge Zn-based aqueous batteries via interfacial adsorption of ion-oligomer complexes. *Nat. Commun.* **2022**, *13* (1), 2283.
(7) Chen, R.; Zavalij, P.; Whittingham, M. S. Hydrothermal Synthesis and Characterization of K x MnO2⊙ y H2O. *Chem. Mater.* **1996**, *8* (6), 1275−1280.
(8) Thackeray, M. M. Manganese oxides for lithium batteries. *Prog. Solid State Chem.* **1997**, *25* (1−2), 1−71.
(9) Li, Z.; Zhang, J. T.; Lou, X. W. Hollow Carbon Nanofibers Filled with MnO2 Nanosheets as Efficient Sulfur Hosts for Lithium-Sulfur Batteries. *Angew. Chem., Int. Ed.* **2015**, *54* (44), 12886−12890.
(10) Liang, X.; et al. A highly efficient polysulfide mediator for lithium−sulfur batteries. *Nat. Commun.* **2015**, *6* (1), 5682.
(11) Zhang, N.; et al. Rechargeable aqueous zinc-manganese dioxide batteries with high energy and power densities. *Nat. Commun.* **2017**, *8* (1), 405.
(12) Pan, H.; et al. Reversible aqueous zinc/manganese oxide energy storage from conversion reactions. *Nature Energy* **2016**, *1* (5), 16039.
(13) Zhong, C.; et al. Decoupling electrolytes towards stable and high-energy rechargeable aqueous zinc−manganese dioxide batteries. *Nature Energy* **2020**, *5* (6), 440−449.
(14) Zhao, J. H.; et al. Highly efficient removal of bivalent heavy metals from aqueous systems by magnetic porous Fe3O4-MnO2: Adsorption behavior and process study. *Chemical Engineering Journal* **2016**, *304*, 737−746.
(15) Yang, R. J.; et al. MnO2-Based Materials for Environmental Applications. *Adv. Mater.* **2021**, *33* (9), 2004862.
(16) Zhu, X.; et al. Superior-performance aqueous zinc-ion batteries based on the in situ growth of MnO2 nanosheets on V2CTX MXene. *ACS Nano* **2021**, *15* (2), 2971−2983.
(17) Gao, Y.; et al. Mn-based oxides for aqueous rechargeable metal ion batteries. *Journal of Materials Chemistry A* **2021**, *9* (19), 11472−11500.
(18) Qiu, C.; et al. Suppressed Layered-to-Spinel Phase Transition in δ-MnO2 via van der Waals Interaction for Highly Stable Zn/MnO2 Batteries. *Small Methods* **2022**, *6* (12), 2201142.
(19) Cui, G.; et al. Synthesis of Nitrogen-Doped KMn8O16 with Oxygen Vacancy for Stable Zinc-Ion Batteries. *Advanced Science* **2022**, *9* (10), 2106067.
(20) Chuai, M.; et al. High-performance Zn battery with transition metal ions co-regulated electrolytic MnO2. *eScience* **2021**, *1* (2), 178−185.
(21) Hu, Y.; et al. Recycling application of Li−MnO2 batteries as rechargeable lithium−air batteries. *Angew. Chem., Int. Ed.* **2015**, *54* (14), 4338−4343.
(22) Zheng, J.; Archer, L. A. Crystallographically Textured Electrodes for Rechargeable Batteries: Symmetry, Fabrication, and Characterization. *Chem. Rev.* **2022**, *122* (18), 14440−14470.
(23) Shin, J.; et al. A review on mechanistic understanding of MnO2 in aqueous electrolyte for electrical energy storage systems. *International Materials Reviews* **2020**, *65* (6), 356−387.
(24) Wang, D.; et al. A superior δ-MnO2 cathode and a self-healing Zn-δ-MnO2 battery. *ACS Nano* **2019**, *13* (9), 10643−10652.
(25) Tang, W.; et al. Sol−gel process for the synthesis of ultrafine MnO2 nanowires and nanorods. *Mater. Lett.* **2014**, *132*, 317−321.
(26) Zhang, X.; et al. Microwave-assisted reflux rapid synthesis of MnO2 nanostructures and their application in supercapacitors. *Electrochim. Acta* **2013**, *87*, 637−644.
(27) Xia, H.; et al. Porous manganese oxide generated from lithiation/delithiation with improved electrochemical oxidation for supercapacitors. *J. Mater. Chem.* **2011**, *21* (39), 15521−15526.
(28) Fan, Q.; Whittingham, M. S. Electrospun manganese oxide nanofibers as anodes for lithium-ion batteries. *Electrochem. Solid-State Lett.* **2007**, *10* (3), A48.
(29) Fan, H.-l.; et al. Hollow carbon microspheres/MnO2 nanosheets composites: hydrothermal synthesis and electrochemical behaviors. *Nano-Micro Letters* **2015**, *7* (1), 59−67.
(30) Chen, B.-R.; et al. Understanding crystallization pathways leading to manganese oxide polymorph formation. *Nat. Commun.* **2018**, *9* (1), 2553.
(31) Darr, J. A.; et al. Continuous hydrothermal synthesis of inorganic nanoparticles: applications and future directions. *Chem. Rev.* **2017**, *117* (17), 11125−11238.
(32) Chen, W.; et al. Effects of particle size on Mg2+ ion intercalation into λ-MnO2 cathode materials. *Nano Lett.* **2019**, *19* (7), 4712−4720.
(33) Tang, Z.; et al. Size-dependent reaction mechanism of λ-MnO2 Particles as cathodes in aqueous zinc-ion batteries. *Energy Material Advances* **2022**, 9765710.
(34) Wei, C.; et al. Preparation and characterization of manganese dioxides with nano-sized tunnel structures for zinc ion storage. *J. Phys. Chem. Solids* **2012**, *73* (12), 1487−1491.
(35) Zeng, Y.; et al. Rationally Designed Mn2O3−ZnMn2O4 Hollow Heterostructures from Metal−Organic Frameworks for Stable Zn-Ion Storage. *Angew. Chem.* **2021**, *133* (49), 25997−26002.
(36) Seo, J. K.; et al. Intercalation and conversion reactions of nanosized β-MnO2 cathode in the secondary Zn/MnO2 alkaline battery. *J. Phys. Chem. C* **2018**, *122* (21), 11177−11185.
(37) Jokerst, J. V.; et al. Nanoparticle PEGylation for imaging and therapy. *Nanomedicine* **2011**, *6* (4), 715−728.
(38) Oziri, O. J.; et al. PEGylation of silver nanoparticles by physisorption of cyclic poly (ethylene glycol) for enhanced dispersion stability, antimicrobial activity, and cytotoxicity. *Nanoscale Advances* **2022**, *4* (2), 532−545.
(39) Wang, Y.; et al. Enhanced dispersion stability of gold nanoparticles by the physisorption of cyclic poly (ethylene glycol). *Nat. Commun.* **2020**, *11* (1), 6089.
(40) Xue, Y.; et al. Physisorption of Poly (ethylene glycol) on Inorganic Nanoparticles. *ACS Nano* **2022**, *16* (4), 6634−6645.
(41) Lang, C. Solvent-non-solvent rapid-injection for preparing nanostructured materials from micelles to hydrogels. *Nat. Commun.* **2019**, *10* (1), 3855 DOI: 10.1038/s41467-019-11804-7.
(42) Rodriguez, F., et al. *Principles of polymer systems*; CRC Press, 2014.
(43) Semenov, A.; Joanny, J.-F.; Khokhlov, A. Associating polymers: equilibrium and linear viscoelasticity. *Macromolecules* **1995**, *28* (4), 1066−1075.
(44) Huang, X.; et al. Highly crystalline macroporous β-MnO2: Hydrothermal synthesis and application in lithium battery. *Electrochim. Acta* **2010**, *55* (17), 4915−4920.
(45) Jiao, F.; Bruce, P. G. Mesoporous crystalline β-MnO2—a reversible positive electrode for rechargeable lithium batteries. *Adv. Mater.* **2007**, *19* (5), 657−660.
(46) Su, D.; Ahn, H.-J.; Wang, G. Hydrothermal synthesis of α-MnO 2 and β-MnO 2 nanorods as high capacity cathode materials for sodium ion batteries. *Journal of Materials Chemistry A* **2013**, *1* (15), 4845−4850.
(47) Reinholdt, M. X.; Babu, P. K.; Kirkpatrick, R. J. Proton Dynamics in Layered Double Hydroxides: A 1H T 1 Relaxation and Line Width Investigation. *J. Phys. Chem. C* **2009**, *113* (24), 10623−10631.
(48) Gadjourova, Z.; et al. Ionic conductivity in crystalline polymer electrolytes. *Nature* **2001**, *412* (6846), 520−523.
(49) Dayie, K. T. Key labeling technologies to tackle sizeable problems in RNA structural biology. *International Journal of Molecular Sciences* **2008**, *9* (7), 1214−1240.
(50) Jenkins, R.; Snyder, R. L. *Introduction to X-ray Powder Diffractometry*; Wiley Online Library, 1996; Vol. *138*.

https://doi.org/10.1021/acsenergylett.3c00018
ACS Energy Lett. 2023, 8, 1744−1751

(51) Xie, G.; et al. The evolution of α-MnO_2 from hollow cubes to hollow spheres and their electrochemical performance for supercapacitors. *J. Mater. Sci.* **2017**, *52* (18), 10915−10926.
(52) Han, S.; Kim, C.; Kwon, D. Thermal degradation of poly (ethyleneglycol). *Polymer degradation and stability* **1995**, *47* (2), 203−208.
(53) Kou, Y.; et al. Thermal analysis and heat capacity study of polyethylene glycol (PEG) phase change materials for thermal energy storage applications. *J. Chem. Thermodyn.* **2019**, *128*, 259−274.
(54) Liu, C.; et al. Expanded hydrated vanadate for high-performance aqueous zinc-ion batteries. *Energy Environ. Sci.* **2019**, *12* (7), 2273−2285.
(55) Yan, M.; et al. Water-lubricated intercalation in $V_2O_5{\cdot}nH_2O$ for high-capacity and high-rate aqueous rechargeable zinc batteries. *Advanced Materials* **2018**, *30* (1), 1703725.
(56) Yang, H.; et al. The origin of capacity fluctuation and rescue of dead Mn-based Zn−ion batteries: a Mn-based competitive capacity evolution protocol. *Energy Environ. Sci.* **2022**, *15* (3), 1106−1118.
(57) Wu, X.; et al. Diffusion-free Grotthuss topochemistry for high-rate and long-life proton batteries. *Nature Energy* **2019**, *4* (2), 123−130.

https://doi.org/10.1021/acsenergylett.3c00018
ACS Energy Lett. 2023, 8, 1744−1751